PCCP

ROYAL SOCIETY OF CHEMISTRY

PAPER

Published on 15 June 2026
Licence and permissions

Check for updates

Cite this: *Phys. Chem. Chem. Phys.*, 2026, **28**, 16661

Elucidation of the structural and magnetic properties of the anion-radical salt (Et-3,5-diMe-Pz)(TCNQ)$_2$

Erik Čižmár,*[a] Mariia Holub,†[a] Daniela Šoltésová,[a] Vladimír Tkáč,[a] Petr Doležal,[b] Dominik Kriegner,[bc] Václav Eigner,[c] Michal Dušek,[c] Dmitry Ziolkovskiy,[d] Mark W. Meisel[ae] and Alexander Feher[a]

Received 13th February 2026,
Accepted 1st June 2026

DOI: 10.1039/d6cp00542j

rsc.li/pccp

The intriguing structural and magnetic properties of the low-dimensional, chain-like anion-radical salt (Et-3,5-diMe-Pz)[TCNQ]$_2$, where Et-3,5-diMe-Pz is *N*-ethyl-3,5-dimethylpyrazinium and TCNQ is 7,7,8,8-tetracyanoquinodimethane, are reported. The nature of the low-temperature transition near 164 K, which may be misidentified as a traditional spin-Peierls event, is clarified with X-ray diffraction, magnetometry, specific heat studies, and numerical calculations. Specifically, this complex is identified as a spin-Peierls-like system due to a subtle intrinsic magnetic dimerisation present at room temperature. The dimerisation of the antiferromagnetic spin chains in (Et-3,5-diMe-Pz)[TCNQ]$_2$ predicted by DFT calculations is much stronger in the low-temperature phase (α = 0.087) than in the high-temperature phase (α = 0.628), as observed in the magnetic properties.

1. Introduction

Charge transfer systems possess an expansive set of possible physical properties, so depending on their composition and structure, they may be classified as insulators, semiconductors, metals, and even superconductors. This electronic diversity, which provides opportunities for structural and magneto-elastic tuning, makes these materials attractive choices when designing devices for practical applications, such as solid electrolytes in electrolytic capacitors, the fabrication of junctions in silicon or cadmium sulphide-based semiconductor devices, or purely organic electronics components, *e.g.* transistors, for analytical purposes in the detection of drugs or harmful substances, ink-jet printed organic electrodes, *etc.*[1–5] In fact, anion-radical salts (ARS) based on 7,7,8,8-tetracyanoquinodimethane (TCNQ) molecules offer fascinating options, since their flat structure is susceptible to π–π stacking, which facilitates the formation of various low-dimensional magnetic systems[3,6–9] with possible applications in spintronics[10–12] and quantum information processing technologies.[13,14] The resulting magnetic interactions are intimately connected with the crystal structure, so even small lattice variations can cause significant changes in magnetic behaviour.[15–19] Therefore, a spin-Peierls (sP) transition often occurs in ARS complexes based on TCNQ as a consequence of strong structural and spin correlations between adjacent molecules.[20–22] Specifically, one-dimensional Heisenberg antiferromagnetic (AFM) chains can undergo a transition to the spin-dimerised state.[23,24]

Herein, structural identification, magnetic, electrical transport, and thermodynamic characterisation of ARS (Et-3,5-diMe-Pz)(TCNQ)$_2$ (where Et-3,5-diMe-Pz is *N*-ethyl-3,5-dimethylpyrazinium) are presented. The crystal structure was established by X-ray diffraction (XRD) techniques at 250 K and 95 K, with additional data acquired during cooling and heating through the transition near 164 K. These data identify the high-temperature (HT) and low-temperature (LT) phases. In addition, a cusp near the transition temperature was observed in the specific heat study. Magnetic properties were investigated and analysed using a model of alternating exchange (or dimerised) Heisenberg AFM chain with spin S = 1/2. Together, these experimental data motivate and empower DFT studies that clarify the magnetic nature of the HT and LT phases. Ultimately, the system is classified as an sP-like system, reminiscent of (o-Me$_2$TTF)$_2$NO$_3$,[9] since at high temperatures the system is tetramerised (magnetically dimerised) with

[a] *Institute of Physics, Faculty of Science, P. J. Šafárik University, Park Angelinum 9, 040 01 Košice, Slovakia. E-mail: erik.cizmar@upjs.sk*
[b] *Department of Condensed Matter Physics, Faculty of Mathematics and Physics, Charles University, Prague, Czech Republic*
[c] *Institute of Physics of the Academy of Sciences of the Czech Republic, Prague, Czech Republic*
[d] *Department of Chemistry, V.N. Karazin Kharkiv National University, Kharkiv, Ukraine*
[e] *Department of Physics and National High Magnetic Field Laboratory, University of Florida, Gainesville, FL 32611-8440, USA*
† Present address: Faculty of Physics and Applied Computer Science, AGH University of Krakow, al. A. Mickiewicza 30, 30-059 Kraków, Poland.

disorder in the cation subsystem, while cooling below 164 K, the cations structurally order while the spins become more dimerised. At low temperatures, the magnetic response is consistent with the description provided by Bulaevski for a dimerised Heisenberg AFM spin chain.[24,25]

2. Experimental and numerical methods

2.1. Synthesis

The synthesis of (Et-3,5-diMe-Pz)$(TCNQ)_2$ (**1**) was performed similarly to that described by Kazheva *et al.*[26] The constituents were obtained from Sigma-Aldrich, and the TCNQ was purified by vacuum zone sublimation. Ethyl iodide was synthesised using a reaction of ethanol with phosphorous triiodide, followed by distillation in an inert medium. To prepare the cation precursor, 2,6-diMe-Pz (2,6-dimethylpyrazine) was quaternized by ethyl iodide in dry acetonitrile under an Ar atmosphere. The resulting *N*-ethyl-3,5-dimethylpyrazinium iodide was recrystallised from acetonitrile. In a separate step, TCNQ was dissolved in acetone at approximately 40 °C to give a nearly saturated solution. The iodide salt was added to this solution with stirring in a 1.5 : 2 molar (iodide:TCNQ) ratio, and the reaction mixture was allowed to cool to room temperature. A black–violet precipitate of the ARS formed, which was filtered, washed with an ether–acetone mixture and ether, and dried under vacuum. Single crystals were obtained by slow evaporation of an acetone solution of the product (crystals of a size of up to 3 × 1.5 × 0.5 mm^3 were obtained). Infrared and Raman spectra, including optical conductivity spectra, were previously reported by Barszcz *et al.*[27] (reported there under the previous naming convention as (*N*-Et-2,6-diMe-Pz)$(TCNQ)_2$).

2.2. X-ray diffraction

A crystal of **1** was mounted on a glass fibre and analysed using a Rigaku OD SuperNova Diffractometer, equipped with an Atlas S2 CCD detector. XRD data were collected using mirror-monochromated Cu-Kα radiation (λ = 1.54184 Å). Data reduction, scaling, and absorption correction were performed using CrysAlisPRO software.[28] The structures were solved by charge flipping using the programme Superflip[29] and refined by full-matrix least-squares on F^2 in Jana2006.[30] The residual electron density maps were visualised using MCE.[31] All hydrogen atoms were discernible in difference Fourier maps and could have been refined to reasonable geometry, but according to common practice, they were kept in ideal positions with C–H = 0.96 Å and U_{iso} (H) set to 1.2 U_{eq} (C). All non-hydrogen atoms were refined using harmonic refinement. The crystal structure was studied at two temperatures, 250 K and 95 K. In the HT phase, the disordered ethyl group was observed, and its bond lengths were restrained to the values observed in the non-disordered LT phase. The occupancies of disordered positions were refined with the sum of occupancies constrained to 1, resulting in an occupancy ratio of 67 : 33. For further information on data collection and structure refinement, see Table S1 (SI). Structural plots were prepared using Diamond software.[32]

The measurement of symmetric ω–2θ scan was performed on a diffractometer, D500-HR-4K, equipped with a position sensitive detector–Mythen in Bragg–Brentano geometry. The sample was placed on a sapphire holder in a ColdEdge cryostat in a helium atmosphere. The sapphire holder was mounted on a ''cold finger'' of a Gifford-McMahon (GM) refrigerator, and over the range of 4 K to 300 K, the temperature measurement was provided by a thermometer placed close to the holder. The sample temperature was measured with an uncertainty lower than 0.5 K and stabilised at ±0.1 K, while the cooling/heating between the temperature set points was 1 K min^{-1}. The monocrystalline sample was oriented on the holder to allow the temperature dependence of the (001) plane distance to be investigated. This geometry of the sample allowed for measuring the low-2θ 00l diffraction maxima: 001, 002, 003, 004, and 005. The 2θ profiles were fitted using the p-Voigt function to determine the peak position, and the Cohen–Wagner plot was used to determine the d_{001} distance. This procedure was used to correct the experimental sample height misalignment, particularly when only low 2θ diffraction maxima were available during measurement.

2.3. Magnetic, specific heat, and resistivity measurements

Measurements of magnetic properties were made using a Quantum Design MPMS3 superconducting quantum interference device (SQUID) magnetometer on the as-prepared polycrystalline sample. The temperature dependence of magnetic susceptibility was measured in the temperature range of 1.8–300 K in magnetic fields of 0.1 T, 0.5 T, and 5 T. The isothermal magnetisation (1.8 K) was investigated up to 7 T. The sample was packed in a clear gelatin capsule held by a plastic straw. The susceptibility data were corrected for the diamagnetic contributions of the background (gelatin capsule) and sample. The diamagnetic contribution of the background was measured in a separate experiment and subtracted from the temperature dependence of the raw magnetic moment. The core diamagnetic susceptibility was estimated using Pascal's constants,[33] and $\chi_{dia} = -1.25 \times 10^{-9}$ m^3 mol^{-1} was subtracted from the measured response.

The measurement of specific heat was performed on a single crystalline sample, 0.71 mg, using Quantum Design PPMS in the temperature range from 200 K to 155 K in a zero magnetic field in the cooling cycle using a slow rate of 0.1 K min^{-1} to avoid significant sample fracturing through the transition temperature region. Due to the nature of the observed structural transition, the sample was also broken on several occasions when the transition region was approached in the electrical resistivity measurements. Therefore, only a simple two-point contact method was used, instead of the four-point method, to successfully measure the resistivity in a cooling cycle with a thermal sweep rate of 0.1 K min^{-1} from 300 K to 179 K, when the crystal breaks. Nevertheless, small discontinuities in the temperature dependence of the resistivity appear below 240 K as evidence of microfractures formed in the crystal,

which contribute to the grain-boundary resistance, especially below 190 K. The PPMS instrument provided temperature control during the two-point contact study of electrical resistivity using a Keithley 6517B electrometer/high resistance meter due to the large resistance of the sample ($\approx$20 kΩ at 300 K, but $\approx$1.6 MΩ at 200 K). Silver wires and paste were used to make the contacts.

2.4. Computational details

Calculations were performed using the ORCA 5.0.4 computational package.[34] Broken-Symmetry (BS) DFT[35] was performed using B3LYP and M06 exchange–correlation functionals[36–38] with triple-ζ basis set Def2-TZVP[39] for all atoms. The resolution-of-the-identity approximation and the chain-of-spheres approximation to exact exchange[40] were applied to speed up the calculations with the appropriate auxiliary basis sets.[41] The TightSCF criteria were applied for the convergence of the self-consistent field (SCF) theory. In the simplest case, the exchange interaction was obtained using Yamaguchi's formalism[42] where

$$J_{BS} = -\frac{E_{HS} - E_{BS}}{\langle S^2\rangle_{HS} - \langle S^2\rangle_{BS}} \quad (1)$$

from a single-point approach (using the X-ray determined structure) with the Hamiltonian

$$\hat{\mathcal{H}} = -2J_{BS}\hat{S}_1\hat{S}_2 \quad (2)$$

The energy E_{HS} corresponds to the high-spin (HS) configuration of two interacting spins in the molecule (parallel orientation of the spins), while the energy E_{BS} corresponds to the broken-symmetry (BS) configuration of those two spins when one of them is flipped (antiparallel orientation of spins). This simple approach can be used only for a pair of spins, so an appropriate fragment with two spins was selected from the chain-like spin structure. Note that the exchange Hamiltonian used for the analysis of the experimental data and the reporting of the calculated J values has the form

$$\hat{\mathcal{H}} = J\hat{S}_1\hat{S}_2 \quad (3)$$

Spin density plots were prepared using Chemcraft software.[43]

3. Results and discussion

3.1. Structure and thermal evolution

The crystallographic data and bond lengths of **1** are reported in Tables 1 and 2 and Tables S1–S5 (SI). The crystal structure is formed by a crystallographically independent cation (Et-3,5-diMe-Pz)$^+$ and two types of anion radicals, specifically TCNQ (A and B), with a disordered ethyl group of the cation in the HT phase (see Fig. 1). As the temperature decreases approaching the LT phase, the ethyl groups become ordered, accompanied by a contraction of the unit cell along all three crystallographic axes, while the crystal structure retains the same space group $P\bar{1}$.

Table 1 Crystal structure data for **1**

Empirical formula	$C_{32}H_{21}N_{10}$	
Formula mass (g mol^{-1})	545.6	
	T = 250 K	T = 95 K
Crystal system	Triclinic	Triclinic
Space group	$P\bar{1}$	$P\bar{1}$
a/Å	7.9282(2)	7.8658(3)
b/Å	13.3615(4)	13.1568(5)
c/Å	14.0733(4)	13.8695(4)
α/°	92.407(2)	89.380(3)
β/°	78.061(2)	76.884(3)
γ/°	77.177(2)	80.584(3)
Cell volume/Å^3	1416.15(7)	1378.54(9)
Z	2	2

Table 2 Characteristic distances between anion-radicals in **1** - interplanar separation of aromatic rings d, ring centroid distance d(Cg···Cg), and ring centroid offset (slippage)

TCNQ pair	d (Å)	d(Cg···Cg) (Å)	Slippage (Å)
HT phase			
AA	3.5674	4.0550(1)	1.9278
AB	3.1740	3.7667(1)	1.9699
BB	3.3558	3.8172(1)	1.8195
LT phase			
AA	3.4560	4.0421(2)	2.0904
AB	3.1316	3.7326(2)	2.0069
BB	3.2155	3.3782(1)	1.0325

In both phases, the formation of layers was observed with the ABBA stacking sequence, resulting in three types of π–π interactions, A–A, A–B, and B–B. Layers of anion radicals

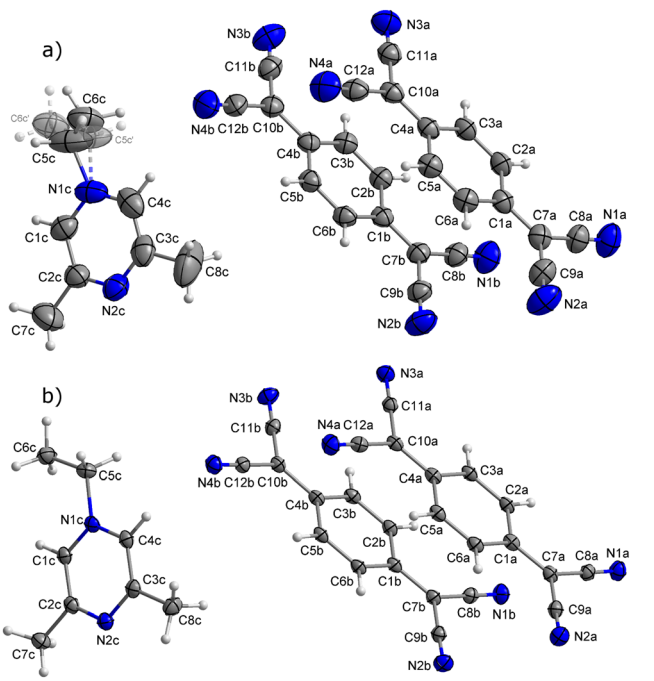

Fig. 1 Molecular structure of **1** including an atom numbering scheme for (a) HT phase, (b) LT phase. The ADPs (anisotropic displacement parameters) are drawn at 50% probability.

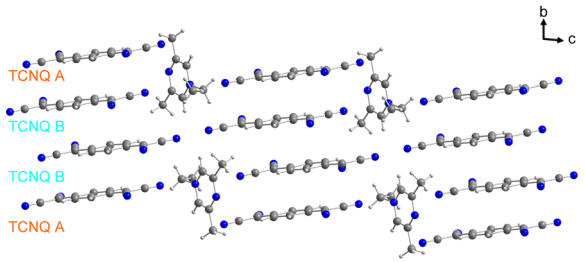

(a) 250 K - HT phase (the weakly occupied atoms of disordered cation are omitted for clarity)

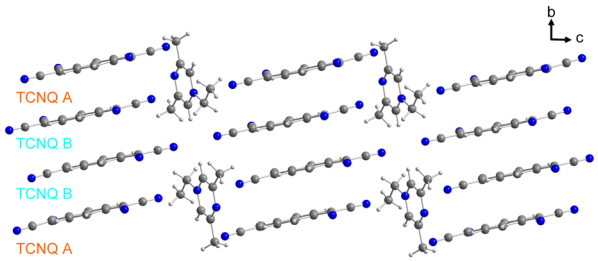

(b) 95 K - LT phase

Fig. 2 The crystal structure of **1** in direction [100] showing ABBA stacking sequence.

alternate with cation sequences along the *c*-axis, Fig. 2. The mean planes of A and B are inclined with an interplanar angle of 2.22(3)° in the HT phase and 0.50(2)° in the LT phase. In both phases, anion radicals are almost perfectly planar, with the highest deviations from planarity of 0.081(2) Å for TCNQ A (N2a) and 0.036(2) Å for TCNQ B (N4b) in the HT phase and 0.1080(12) Å for TCNQ A (N2a) and 0.0657(12) Å for TCNQ B (N1b) in the LT phase. The shortest interplanar separation between anion radicals and C···C interactions between anion radicals in the stacks are, in both phases, the longest for A–A and shortest for A–B (see Table 2 and Table S3 (SI), and Fig. 3), creating structural tetramers of ABBA type. Additional information also provides the distance between the ring centroids and their offsets (slippage) (Table 2, Fig. 3), which show an interesting behaviour when comparing HT and LT phases. Although interplanar separation and C···C interactions are shortest

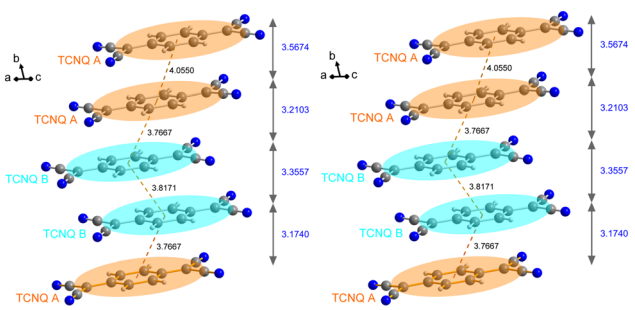

(a) 250 K - HT phase (b) 95 K - LT phase

Fig. 3 Stacks of TCNQ anion-radicals with interplanar separation and distance between ring centroids (Å).

between A–B pairs in both phases, the ring centroid distance and slippage become shortest for the B–B pair in the LT phase.

The estimation of charge distribution along the stacks is crucial information for the subsequent interpretation of the magnetic data. Because the charge localisation on the TCNQ molecule is correlated with its overall geometrical structure, the analysis of the bond lengths in TCNQ provides the required insight. Specifically, using the Kistenmacher relationship,[44] as reported in Table S6 (SI), one obtains the results that TCNQ A and TCNQ B carry the charge of 0.571*e* and 0.451*e*, respectively, at 250 K. The charge distribution is slightly different at 95 K, according to the bond lengths obtained from XRD, TCNQ A and TCNQ B carry the charge of 0.637*e* and 0.295*e*, respectively. As a result, the A–B pair creates a structural dimer $(TCNQ)_2^{\bullet -}$ with effective spin $S = 1/2$ in both phases.

In addition to π–π stacking in ABBA sequence, the crystal structure of **1** is stabilised by weak hydrogen bonds of C–H···N type between the adjacent TCNQ stacks and between TCNQ anions and cations, as shown in Fig. 4 and summarised in Tables S4 and S5 (SI) to form a 3D structure in both, HT and LT, structures. The change in the structure through the phase transition connected with the disorder–order change of cation ethyl groups also includes the possibility of a change in the hydrogen bonding network, forming a more dense hydrogen bond network in the LT phase.

Although the crystal structures maintain the same symmetry at 250 K and 95 K (the space group is $P\bar{1}$; the difference is mainly due to the disorder of the ethyl group in the HT phase), it is not clear whether the ordering is continuous or a rather sharp transition. To elucidate this, another X-ray experiment was performed, where the temperature dependence of the 001 diffraction maxima was measured in fine temperature steps. XRD data were collected during two cooling and warming cycles (see Fig. 5 and 6). Thermal cycles provide insight into the mechanism of the transition. The transition is step-like, with a clear discontinuity in the lattice parameters, but the sample does not transform at a single temperature. Instead, a distinct coexistence of the LT and HT phases is observed. The width of the coexistence interval is approximately 6 K; see Fig. 5. To track the hysteresis of the transition, it is necessary to identify the temperature at which the same phase fraction appears during both cooling and heating, giving the hysteresis of 15 K; see Fig. 6. Interestingly, d_{001} first increases with the decreasing temperature from 300 K to 150 K, then drops to a lower value in the LT phase and slightly decreases, reaching a minimum value of 13.49 Å at 10 K, as seen in Fig. 6. The high-resolution X-ray data are compared with the results of standard single-crystal diffraction experiments performed at 250 and 95 K, showing good agreement; see Fig. 6.

3.2. Magnetic data

The temperature dependence of the low-field magnetic susceptibility increases with decreasing temperature from room temperature to nominally 174 K (see Fig. 7). Upon further cooling, a transition reminiscent of a sP-like transition occurs below 174 K. At temperatures below 20 K, the

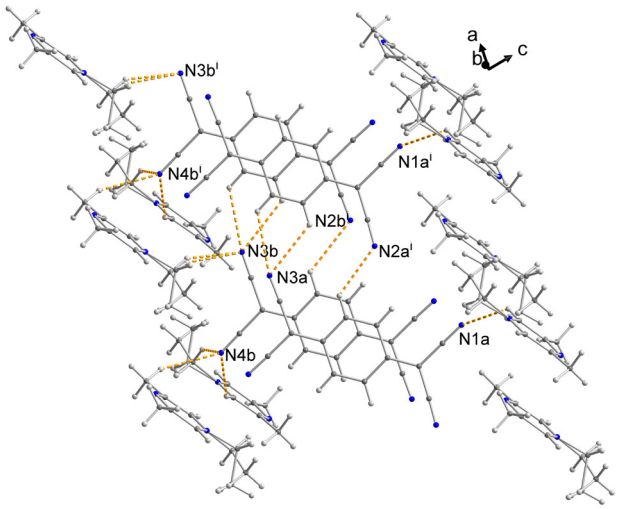

(a) 250 K - HT phase including disordered cations

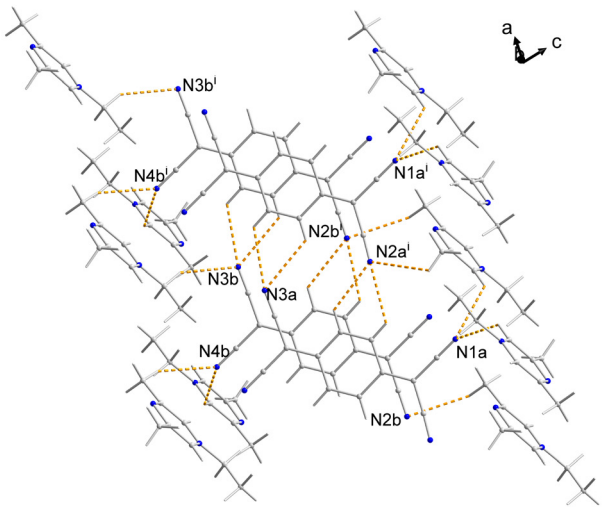

(b) 95 K - LT phase

Fig. 4 Hydrogen bonding system in **1**, possible weak hydrogen bonds are represented by orange dashed lines. For the sake of clarity, only labels for acceptor atoms are shown. Symmetry codes: (i) 1 + *x*, *y*, *z*.

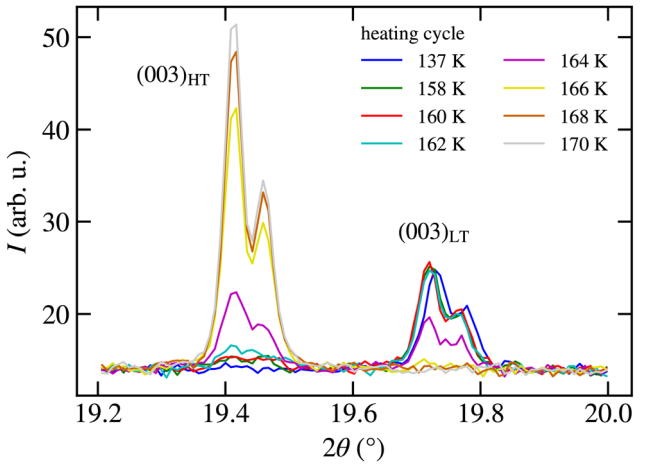

Fig. 5 Temperature dependence of 003 diffraction maxima of **1** measured during heating, showing the coexistence of both phases at 164 K.

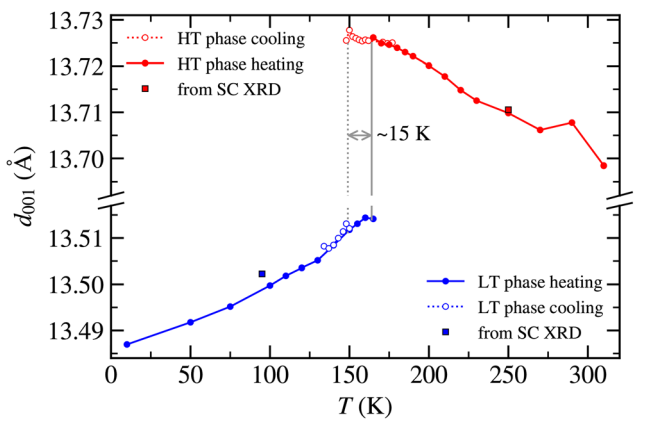

Fig. 6 Temperature dependence of the d_{001} lattice-plane spacing. Red and blue colours denote the HT and LT phases, respectively. Filled and open symbols correspond to heating and cooling cycles. Square symbols represent calculated values based on lattice parameters obtained from single-crystal diffraction measurements at 250 K and 95 K. The hysteresis between cooling and heating is approximately 15 K.

signal increases again with decreasing temperature, and this Curie-like increase is typically associated with the paramagnetic behaviour of isolated spins in the complex (non-bonded $(TCNQ)_2^{\bullet-}$), end-chain spins or topological defect-induced moments referred to as pinned solitons[13,45] in dimerised chains. Thermal hysteresis, similar to the XRD study, was also observed in the magnetic response during the thermal cycling between 180 K and 140 K, as shown in Fig. S1a (SI). These data are presented for an applied magnetic field of 5 T, and the width of the hysteresis was observed to be independent of the strength of the applied field.

In fact, the transition below 174 K is not a typical sP ordering event, because the XRD data have shown that the HT structure is also tetramerized (magnetically dimerised), but with disorder in the cation subsystem. In other words, this complex is a rare example of an sP-like system. At transition temperature, the structural disorder in the cation subsystem of **1** is removed and the magnetic dimerisation is enhanced, as shown in Fig. 3. In contrast to the typical sP transition with a uniform AFM spin chain description above the transition, the magnetism of both HT and LT phases of **1** requires the description using an alternating exchange Heisenberg AFM chain model (hereafter also called the dimerised AFM chain model) for both phases, but with different dimerisation ratios. In both phases, the magnetic behaviour is primarily governed by the singlet–triplet excitation spectrum. In the LT phase, triplet excitations begin to emerge only at higher temperatures (but below the transition temperatures), whereas in the HT phase, triplet excitations are already strongly populated. The sP transition temperature in a similar temperature range was also observed in other ARS, $KTCNQF_4$[46] and $(o\text{-}Me_2TTF)_2NO_3$.[9] The eventual structural order–disorder

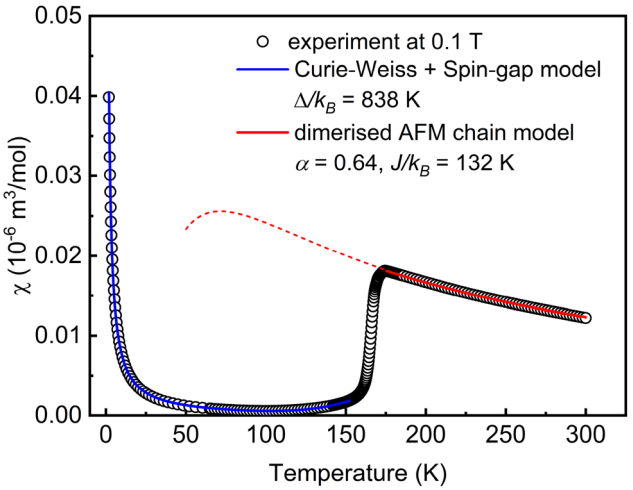

Fig. 7 The magnetic susceptibility of **1** with models for LT and HT phases measured during heating. The red dashed line represents the extrapolation of the dimerised AFM chain model from the HT phase into the LT region.

transition in similar ARS is connected with the appearance of the sP transition,[47,48] while in some cases the order–disorder transition is decoupled from the sP transition,[9,49,50] which appears at lower temperatures. In a well-studied MEM(TCNQ)$_2$, the order–disorder transition at 335 K is related to a change in electric conductivity, while magnetically the system remains a uniform AFM spin chain down to 19 K, where the sP transition appears.[20,51]

A behaviour very similar to **1** has been observed in TEA(TCNQ)$_2$ with a structural transition at 220 K, where it is assumed that the TEA cations freeze from the disordered HT state into one of two possible orientations with random occupancy,[52] resulting in a description of the transition as one from static to dynamic disorder. This transition is also manifested by an anomaly in electrical conductivity,[53] susceptibility,[54] and dielectric spectroscopy.[55] Below this transition, a gradual opening of a spin gap, reminiscent of the sP transition, was observed. New muon spin spectroscopy studies show evidence of 3D AFM Ising order of defect-induced paramagnetic moments in dimerised phase of TEA(TCNQ)$_2$ below 120 K.[56] It is worth mentioning that a similar magnetic ordering, but of the Heisenberg universality class, was observed in KTCNQF$_4$.[46] The magnetic dimerisation in **1** appears to be more abrupt than in TEA(TCNQ)$_2$, tentatively assigned to the full ordering of cations in the temperature range 150–175 K as shown in Fig. 6, leaving no randomness in TCNQ stacks. In addition, we were unable to detect any significant anomalies in the magnetic data in the dimerised phase (see Fig. S1b (SI)) similar to KTCNQF$_4$[57] connected with 3D magnetic correlations. On the other hand, the creation of AFM spin pairs was shown in (*o*-DMTTF)$_2$X salts from magnetic and electron paramagnetic resonance experiments,[58] which will be discussed further.

3.3. Resistivity and specific heat studies

In the case of the Peierls transition in conductive ARS, the change from metallic to semiconductive (or insulating) character of the electrical conductivity occurs below the transition temperature, while the system remains semiconductive through the transition in typical examples of the sP transition in CuGeO$_3$,[59] TiOCl[60] or MEM(TCNQ)$_2$.[20,51] Thus, the temperature dependence of the electrical resistivity in the HT phase was measured along the *b**-axis, in anion-radical layers approximately along the TCNQ stacks as shown in Fig. S2 (SI), to distinguish the character of the transition. The temperature dependence of the resistivity ρ possesses a semiconducting character, Fig. S3 (SI), suggesting that the structural transition is not connected with the Peierls transition.

The charge transport in organic compounds can be described by different models, such as the classical band transport or various hopping transport models.[61] A delocalised molecular wave function is expected with mean free paths larger than the inter-site distance within the band transport model; the hopping mechanism is described by tunnelling or overcoming potential barriers between localised sites, with the mean free path of the order of the inter-site distance. The temperature dependence of resistivity of **1** has an Arrhenius-type character (see the inset of Fig. S3 (SI)); thus, the band transport model was applied in the form

$$\rho(T) = \rho_0 \mathrm{e}^{-\Delta E\left(\frac{T-T_0}{k_B T\, T_0}\right)} \quad (4)$$

in the temperature range of 190–300 K with T_0 = 300 K and ρ_0 = 0.27 Ωm (conductivity σ_0 = 0.037 S cm^{-1}), yielding the activation energy ΔE = 0.224 eV. The estimated activation energy is slightly smaller, ΔE = 0.213 eV in the temperature range down to 240 K, where the first microfractures in the crystal appear, which would eventually increase the resistivity similar to compacted polycrystalline samples. Comparison with other TCNQ-based ARS shows that while the room-temperature conductivity of metallic ARS, such as TTF-TCNQ, may reach 500 S cm^{-1},[62,63] many ARS reported by Melby *et al.*[64,65] reach only 10^{-5}–10^{-4} S cm^{-1}, and well-studied TEA(TCNQ)$_2$ in the thermally activated conductivity phase has a conductivity of 5.7 S cm^{-1}.[66] The room-temperature conductivity of the same family of ARS can differ by several orders depending on the stacking of TCNQ radicals, from 3.9 × 10^{-5} S cm^{-1} for dimerised TCNQ in stacks to 0.024 S cm^{-1} for the uniform TCNQ spacing.[26] Thus, the estimated conductivity in **1** agrees well with a weaker dimerisation observed in the HT phase.

In addition, the temperature dependence of specific heat was investigated in a zero magnetic field over the temperature range of 156 K to 200 K, Fig. S4 (SI), to track the structural phase transition. A cusp-like anomaly was observed near 164 K, which corresponds to the transition temperature as deduced from the XRD measurements presented in Fig. 5.

3.4. Theoretical calculations and analysis of magnetic data

To obtain insight into the magnetic nature of the HT and LT phase of **1**, BS DFT calculations were performed, using the B3LYP and M06 exchange–correlation functionals, which provide the dimerisation ratio $\alpha = J_2/J_1$ of two successive nearest-neighbour exchange interactions in the anion-radical stacks of the single-crystal data at 250 K and 95 K. Although B3LYP is

widely used in BS DFT calculations, M06 has been suggested to perform well in calculating intermolecular exchange interactions, *e.g.*, transmitted through π–π contacts.[67–69] Since the structure consists of infinite chains (stacks), each exchange interaction calculation focused on one fragment consisting of a pair of $(TCNQ)_2^{\bullet-}$ units representing $J_1 = J(1+\delta)$ and $J_2 = J(1-\delta)$ in the dimerised Heisenberg AFM spin chain described by the Hamiltonian

$$\mathcal{H} = J\sum_i \left[(1-\delta)\hat{S}_{2i-1}\cdot\hat{S}_{2i} + (1+\delta)\hat{S}_{2i}\cdot\hat{S}_{2i+1}\right]. \quad (5)$$

First, the HS state energy was calculated, then one of the spins residing on a $(TCNQ)_2^{\bullet-}$ unit was flipped (the spin density obtained from the HS calculation was inverted), and the BS state energy was calculated, yielding the Heisenberg exchange interaction of eqn (1). The calculations were performed on two model structures for each temperature, namely simplified structures containing four anion-radical molecules surrounded by eight nearest cations without (sm - small model molecule, Fig. 8) and then four anion-radical molecules surrounded by twelve nearest cations without (lm - large model molecule, Fig. S5 (SI)), this notation is used Table 3. Since the structural disorder of the ethyl group of the cation complicates the calculations for the structure at 250 K, the model structure only included the atom positions of the ethyl group with higher probability.

Since calculations are based on the electron and spin density distributions for different types of model structures, the spin density of the BS states is shown in Fig. 8 and Fig. S5 (SI). The energy of the BS state can also be minimised when the spin distribution residing on different atoms in the model structure is evenly distributed and averaged to zero in the whole model structure, Fig. 8 and Fig. S5 (SI) show a distinct distribution of up (orange) and down (blue) spin density in $(TCNQ)_2^{\bullet-}$ units. In general, the results summarised in Table 3 indicate that, in both temperature regions, the system remains in a dimerised state, which justified its classification as sP-like. The dimerisation parameters α and δ are reported in Table 3 together with the energy gap $\Delta = 2J\delta^{3/4}$.[70–72] The magnitude of the exchange interactions is well correlated with the interplanar distance of the neighbouring TCNQ molecules in the stacks shown in Fig. 3, and we can assign J_1 and J_2 to AB-BA and BA-AB pairs, respectively. As a result, the expected spin chain dimerisation in the LT phase with an average value of $\alpha = 0.087$ is much stronger than in the HT phase with $\alpha = 0.628$ (excluding the result for lm, B3LYP method). The predicted large energy gap in the LT phase would yield a significant reduction in the magnetic moment below the transition temperature, as observed in the magnetic data in Fig. 7.

Table 3 Result of the BS DFT calculations using the B3LYP and M06 functionals for $(TCNQ)_2^{\bullet-}\cdots(TCNQ)_2^{\bullet-}$ model structures (sm - small model molecule, lm - large model molecule)

Temp (K)	Model	J_1/k_B (K)	J_2/k_B (K)	α	δ	Δ/k_B (K)
250	sm, B3LYP	140.8	92.1	0.654	0.209	72
250	sm, M06	240.6	138.3	0.575	0.270	142
250	lm, B3LYP	88.0	33.0	0.375	0.455	102
250	lm, M06	132.1	86.7	0.656	0.208	67
95	sm, B3LYP	1870.9	149.4	0.080	0.852	1792
95	sm, M06	1889.6	168.2	0.089	0.837	1800
95	lm, B3LYP	1570.9	131.4	0.084	0.845	1501
95	lm, M06	1599.6	151.8	0.095	0.827	1518

Despite the prediction of magnetic dimerisation present in both phases from the DFT calculations, the temperature dependence of susceptibility needs to be analysed separately in the HT and LT regions. The decrease in the susceptibility with increasing temperature suggests that a maximum in the temperature dependence of the susceptibility predicted for the dimerised AFM spin chain would lie at lower temperatures. Thus, experimental data in the HT phase in Fig. 7 were fitted using the high-temperature series expansion for the dimerised AFM spin chain (eqn (5)) with a dominant exchange interaction J_1 and the degree of dimerisation described by the parameter α.[73,74] In this description, the magnetic susceptibility may be written as

$$\chi(T) = \frac{N_A\mu_B^2 g^2}{k_B T}\frac{A + Bx + Cx^2}{1 + Dx + Ex^2 + Fx^3} \quad (6)$$

where N_A is the Avogadro constant, k_B is the Boltzmann constant, μ_B is Bohr magneton, the g-factor is $g = 2$ for TCNQ, $x = J_1/(k_BT)$, and α is included in the coefficients A to F.[75] This expression yields the theoretical result for the uniform Heisenberg AFM spin chain for $\alpha = 1$.[72,76] The result of $\alpha = 0.64$ and $J_1/k_B = 132$ K, shown in Fig. 7, is consistent with the aforementioned DFT calculations. On the other hand, a possible distribution of exchange couplings in the HT phase needs to be considered; therefore, only an effective coupling is extracted using eqn (6). Since the susceptibility maximum expected at low temperatures is not observable (an extrapolation of this temperature dependence into the LT range is shown in Fig. 7 by the dashed line), a satisfactory fit is also possible using the uniform Heisenberg AFM chain model with $J/k_B = 121.8$ K.

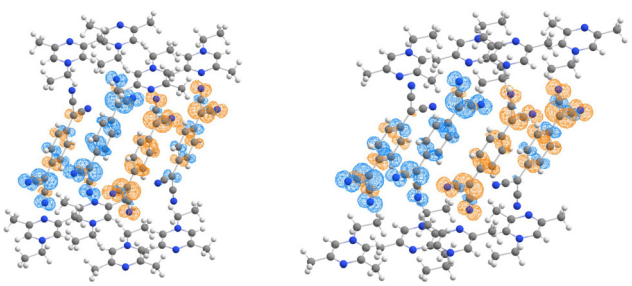

(a) BS1 (b) BS2

Fig. 8 The spin density of the BS states of two small model molecules (sm, Table 3) with four TCNQ anion radicals surrounded by eight nearest cations extracted from the crystal structure of **1** obtained at 95 K. The blue and orange colours of the spin density distribution correspond to the two opposite spin polarisations (isovalue 0.002). Exchange interactions J_1 (corresponding to AB–BA interaction, BS1) and J_2 (corresponding to BA–AB interaction, BS2) were calculated using the BS DFT approach.

Below 150 K, high-temperature series expansion, eqn (6), is not appropriate for the description due to substantial dimerisation, and the susceptibility data were fit using

$$\chi_i(T) = \frac{a}{T^{\gamma}} e^{-\frac{\Delta}{k_B T}} + n\frac{C_{def}}{T-\Theta} + \chi_0 \qquad (7)$$

where the first term represents the LT approximation ($k_B T \ll \Delta$) of the susceptibility of a dimerised AFM spin chain as described by Bulaevski for sP systems with $\gamma = 1/2$.[24,25,72] The next term represents paramagnetic moments of concentration n with a Curie constant C for $S = 1/2$ entities (non-interacting defect-induced moments, thus, assuming Weiss temperature $\Theta = 0$) with $g = 2$, while the last term χ_0 allows for a temperature-independent diamagnetic correction. The fit shown in Fig. 7 is for $n = 0.016$, $a = 14.95 \times 10^{-6}$ emu K$^{1/2}$ mol^{-1}, with an energy gap of $\Delta/k_B = 838$ K, which seems to be underestimated compared to the values obtained from BS DFT calculations, Table 3, but suggesting a very strong magnetic dimerisation in the LT phase. Of course, a direct comparison of the values obtained from the experiment and from two model structures should be taken with caution, since both model structures are just fragments of chains in which the spin density of all neighbouring TCNQ molecules has not been considered. Thus, the differences may be attributed to the simplified model structures used with BS DFT calculations and to the fact that Δ in eqn (7) represents a zero-temperature energy gap value in sP systems, while the energy gap might be temperature dependent. The presence of paramagnetic species at low temperatures was further evidenced by the field dependence of isothermal magnetisation at 1.8 K, which is reasonably well reproduced by a Brillouin function using $n = 0.018$, as shown in Fig. S6 (SI). The contribution of bulk triplet excitations is negligible at such low temperatures and in the presence of a large energy gap, and remains experimentally undetectable up to magnetic fields of 7 T when compared with the defect-induced moments carrying effective spin $S = 1/2$. However, the deviation of the magnetisation curve from the Brillouin function may also indicate the existence of weak AFM interactions between defect-induced moments.

Possible correlations between paramagnetic moments at low temperatures were studied in (*o*-DMTTF)$_2$X, considering the creation of AFM coupled defect pairs.[58] The LT susceptibility of **1** was measured with a higher density of points in the magnetic field of 0.5 T to obtain a sufficiently high magnetic moment, and the temperature dependence of the χT was plotted in the LT region, as shown in Fig. 9. The decrease in susceptibility at the lowest temperatures was attributed to the depopulation of the triplet states of AFM dimers as described by the Bleaney–Bowers model for $S = 1/2$ AFM dimer, including the Curie term, in the form

$$\frac{\chi T}{C} = n_{dim}\frac{1}{2(3+e^{\Delta_S/k_B T})} + \frac{3}{8}(1-n_{dim}) \qquad (8)$$

where Δ_S is a gap between the singlet and triplet state in AFM dimers related (but not equal) to an effective exchange interaction between defect spins, and n_{dim} is the fraction of defect spins forming dimers, C represents the Curie constant of defect spins. The parameters obtained were $n_{def} = 0.16$ and $\Delta_S/k_B = 2.60$ K, suggesting that a relatively high proportion of defects (about 15%) are coupled in AFM dimers, but less than in (*o*-DMTTF)$_2$Br. The extracted gap of 2.6 K is the result of an effective average exchange interaction of $\approx$3 K between defect-induced diluted moments mediated along the stacks, but also between the stacks (presumably due to the short contacts in the *ab*-plane).

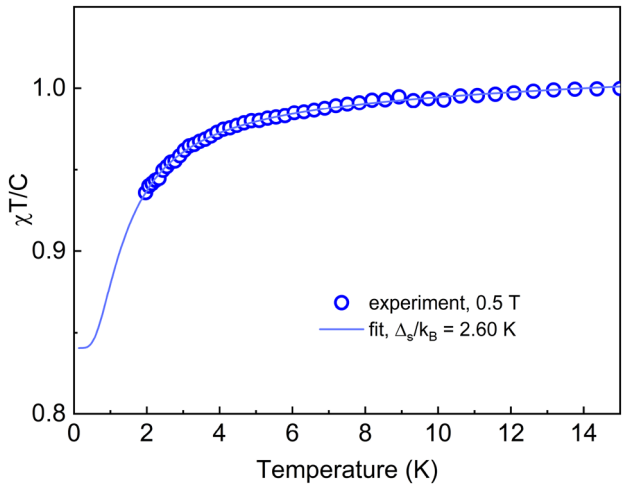

Fig. 9 The low-temperature χT per one mol of defects with $g = 2$ was analyzed using a combination of the Bleaney–Bowers dimer model and Curie contribution of paramagnetic moments.

4. Summary and conclusions

By combining XRD characterisation, magnetic, electrical transport, and specific heat studies with DFT and numerical analysis, the properties of ARS **1** are comprehensively elucidated. The HT and LT phases are both dimerised and the sP-like transition is identified near 164 K, as evidenced by XRD, magnetometry, and specific heat data obtained through the transition. The DFT and numerical analysis clarify the microscopic description as dimerised AFM spin chains, with the strength of the dimerisation changing from weaker to stronger while moving from the HT to the LT phase. The XRD data further clarify the apparent broadness of the transition, which spans from nominally 150 K to 175 K, as arising from a distribution of local environments that govern the specific and discrete transition temperature of the microscopic locale. The characterisation and control of the structural coherence of these microscopic domains and possible LT correlations between the defect-induced spins are beyond the scope of this work and provide a potential challenge to future investigations using spectroscopic methods (electron paramagnetic resonance or muon spin spectroscopy).

Author contributions

Erik Čižmár: investigation, methodology, conceptualisation, writing – review & editing, funding acquisition. Mariia Holub: investigation, data curation. Daniela Šoltésová: investigation,

data curation, writing – original draft preparation. Vladimír Tkáč: data curation, writing – review & editing. Petr Doležal: investigation, data curation, writing – review & editing. Dominik Kriegner: investigation, data curation. Václav Eigner: investigation, data curation, writing – review & editing. Michal Dušek: data curation, writing – review & editing. Dmitry Ziolkovskiy: investigation, data curation. Mark W. Meisel: formal analysis, conceptualisation, writing – review & editing. Alexander Feher: conceptualisation, writing – review & editing.

Conflicts of interest

There are no conflicts to declare.

Data availability

The data supporting this article have been included as part of the supplementary information (SI). Supplementary information: structural parameters and supporting data. See DOI: https://doi.org/10.1039/d6cp00542j.

CCDC 2526797 (250 K) and 2526796 (95 K) contain the supplementary crystallographic data for this paper.[77a,b]

Acknowledgements

This work was supported by the Slovak Research and Development Agency under contract No. APVV-22-0172 and APVV-23-0006. Part of the research results were obtained by using the computational resources of the supercomputer PERUN, operated by the Supercomputing Centre at the Technical University of Košice (TUKE), Slovakia with the support of the European Union from the funds of the Recovery and Resilience Plan of the Slovak Republic within the framework of project No. 17I03-04-P03-00001, Development and design of a supercomputer for the National Supercomputing Center. Low-temperature XRD measurements were performed in MGML (mgml.eu), which is supported within the program of Czech Research Infrastructures (project no. LM2023065). This work was supported by the CzechNanoLab project LM2023051 funded by MEYS CR, which is gratefully acknowledged for the financial support for the measurements/sample fabrication at LNSM Research Infrastructure. The National High Magnetic Field Laboratory (NHMFL or MagLab), which is funded by the National Science Foundation (NSF) Cooperative Agreements DMR-1644779 and DMR-2128556, and the State of Florida, provided partial support for the effort of M. W. M.

References

1 N. Toyota, J. Müller and M. Lang, *Low-Dimensional Molecular Metals*, Springer Berlin, Heidelberg, 1st edn, vol. 154, 2007.
2 W. B. Feng, W. Xu, H. B. Duan and H. Zhang, *RSC Adv.*, 2022, **12**, 32475–32479.
3 V. A. Starodub and T. N. Starodub, *Russ. Chem. Rev.*, 2014, **83**, 391–438.
4 T. Starodub and S. Michalkiewicz, *Materials*, 2024, **17**, 5864.
5 R. Ramanathan, L. L. Martin, A. M. Bond and V. Bansal, *ACS Appl. Nano Mater.*, 2024, **7**, 28057–28073.
6 A. J. Epstein, S. Etemad, A. F. Garito and A. J. Heeger, *Phys. Rev. B*, 1972, **5**, 952–977.
7 L. Ballester, A. M. Gil, A. Gutiérrez, M. F. Perpiñán, M. T. Azcondo, A. E. Sánchez, U. Amador, J. Campo and F. Palacio, *Inorg. Chem.*, 1997, **36**, 5291–5298.
8 D. Jérome, *Chem. Rev.*, 2004, **104**, 5565–5592.
9 O. Jeannin, E. W. Reinheimer, P. Foury-Leylekian, J.-P. Pouget, P. Auban-Senzier, E. Trzop, E. Collet and M. Fourmigué, *IUCrJ*, 2018, **5**, 361–372.
10 V. N. Prigodin, J. W. Yoo, H. W. Jang, C. Kao, C. B. Eom and A. J. Epstein, *J. Phys.: Conf. Ser.*, 2011, **292**, 012001.
11 A. Wang, J. Peng, N. Ren, L. Ding, X. Yu, Z. Wang and M. Zhao, *J. Phys. Chem. Lett.*, 2021, **12**, 7921–7927.
12 Z. Jakub, A. Kurowská, O. Herich, L. Černá, L. Kormoš, A. Shahsavar, P. Procházka and J. Čechal, *Nanoscale*, 2022, **14**, 9507–9515.
13 S. Bertaina, C.-E. Dutoit, J. Van Tol, M. Dressel, B. Barbara and A. Stepanov, *Phys. Rev. B: Condens. Matter Mater. Phys.*, 2014, **90**, 060404.
14 S. Bertaina, C.-E. Dutoit, J. Van Tol, M. Dressel, B. Barbara and A. Stepanov, *Phys. Procedia*, 2015, **75**, 23–28.
15 A. Radváková, D. V. Ziolkovskiy, M. Kajňaková, B. Laskowska, B. Barszcz, A. Graja, V. A. Starodub and A. Feher, *J. Phys.: Condens. Matter*, 2009, **21**, 175405.
16 A. Radváková, O. Kazheva, A. Chekhlov, O. Dyachenko, M. Kucmin, M. Kajňaková, A. Feher and V. Starodub, *J. Phys. Chem. Solids*, 2010, **71**, 752–757.
17 M. Botko, V. Cheranovskii, O. Kazheva, G. Shilov, O. Dyachenko, A. Verkin, M. Kucmin, V. Starodub, A. Radváková, M. Kajňaková and A. Feher, *Solid State Sci.*, 2013, **24**, 85–89.
18 A. I. Taponen, A. Ayadi, M. K. Lahtinen, I. Oyarzabal, S. Bonhommeau, M. Rouzières, C. Mathonière, H. M. Tuononen, R. Clérac and A. Mailman, *J. Am. Chem. Soc.*, 2021, **143**, 15912–15917.
19 A. I. Taponen, A. Ayadi, N. Svahn, M. K. Lahtinen, M. Rouzières, R. Clérac, H. M. Tuononen and A. Mailman, *Cryst. Growth Des.*, 2022, **22**, 7110–7122.
20 S. Huizinga, J. Kommandeur, G. A. Sawatzky, B. T. Thole, K. Kopinga, W. J. M. de Jonge and J. Roos, *Phys. Rev. B: Condens. Matter Mater. Phys.*, 1979, **19**, 4723–4732.
21 T. Sekikawa, H. Okamoto, T. Mitani, T. Inabe, Y. Maruyama and T. Kobayashi, *Phys. Rev. B: Condens. Matter Mater. Phys.*, 1997, **55**, 4182–4190.
22 M. Kajňaková, M. Botko, V. A. Starodub, E. Čižmár and A. Feher, *Acta Phys. Pol., A*, 2014, **126**, 254–255.
23 E. Pytte, *Phys. Rev. B*, 1974, **10**, 4637–4642.
24 L. N. Bulaevskii, *Sov. Phys. Usp.*, 1975, **18**, 131–150.
25 L. N. Bulaevskii, *Sov. Phys. Solid State*, 1969, **11**, 921.
26 O. V. Kazheva, D. V. Ziolkovskiy, G. G. Alexandrov, O. A. Dyachenko, V. A. Starodub, A. V. Khotkevich and G. Y. Vasilets, *Funct. Mater.*, 2006, **13**, 692–696.

27 B. Barszcz, B. Laskowska, A. Graja, D. Ziolkovskiy and V. Starodub, *Synth. Met.*, 2009, **159**, 2486–2490.
28 *CrysAlis PRO*, Agilent Technologies Ltd, Yarnton, Oxfordshire, England, 2014.
29 L. Palatinus and G. Chapuis, *J. Appl. Crystallogr.*, 2007, **40**, 786–790.
30 V. Petříček, M. Dušek and L. Palatinus, *Z. Kristallogr. - Cryst. Mater.*, 2014, **229**, 345–352.
31 M. Hušák and B. Kratochvl, *J. Appl. Crystallogr.*, 2003, **36**, 1104.
32 K. Brandenburg, *Diamond, Crystal Impact*, Bonn, Germany, 2022.
33 G. A. Bain and J. F. Berry, *J. Chem. Edu.*, 2008, **85**, 532.
34 F. Neese, *Wiley Interdiscip. Rev.: Comput. Mol. Sci.*, 2022, **12**, e1606.
35 H. Nagao, M. Nishino, Y. Shigeta, T. Soda, Y. Kitagawa, T. Onishi, Y. Yoshioka and K. Yamaguchi, *Coord. Chem. Rev.*, 2000, **198**, 265–295.
36 A. D. Becke, *J. Chem. Phys.*, 1993, **98**, 5648–5652.
37 Y. Zhao and D. G. Truhlar, *Acc. Chem. Res.*, 2008, **41**, 157–167.
38 Y. Zhao and D. G. Truhlar, *Theor. Chem. Acc.*, 2008, **120**, 215–241.
39 F. Weigend and R. Ahlrichs, *Phys. Chem. Chem. Phys.*, 2005, **7**, 3297–3305.
40 F. Neese, F. Wennmohs, A. Hansen and U. Becker, *Chem. Phys.*, 2009, **356**, 98–109.
41 F. Weigend, *Phys. Chem. Chem. Phys.*, 2006, **8**, 1057–1065.
42 K. Yamaguchi, Y. Takahara and T. Fueno, *Applied Quantum Chemistry*, Dordrecht, 1986, pp. 155–184.
43 *Chemcraft - graphical software for visualization of quantum chemistry computations*, https://www.chemcraftprog.com, Version 1.8, build 748b.
44 T. J. Kistenmacher, T. J. Emge, A. N. Bloch and D. O. Cowan, *Acta Crystallogr. B*, 1982, **38**, 1193–1199.
45 M. Nishino, H. Onishi, K. Yamaguchi and S. Miyashita, *Phys. Rev. B: Condens. Matter Mater. Phys.*, 2000, **62**, 9463–9471.
46 A. Berlie, I. Terry, M. Szablewski and S. Giblin, *Phys. Rev. B*, 2016, **93**, 054422.
47 Z. Tian, H. Duan, X. Ren, C. Lu, Y. Li, Y. Song, H. Zhu and Q. Meng, *J. Phys. Chem. B*, 2009, **113**, 8278–8283.
48 S. Kumeta, T. Kawamoto, T. Shirahata, Y. Misaki and T. Mori, *J. Phys. Soc. Jpn.*, 2016, **85**, 094701.
49 J. P. Pouget and S. Ravy, *J. Phys. I France*, 1996, **6**, 1501–1525.
50 C. Coulon, P. Foury-Leylekian, J. M. Fabre and J. P. Pouget, *Eur. Phys. J. B*, 2015, **88**, 85.
51 M. Morrow, W. N. Hardy, J. F. Carolan, A. J. Berlinsky, L. Weiler, V. K. Gujral, A. Janossy, K. Holczer, G. Mihlay, G. GrÃ¼ner, S. Huizinga, A. Verwey and G. A. Sawatsky, *Can. J. Phys.*, 1980, **58**, 334–342.
52 A. Filhol and M. Thomas, *Acta Crystallogr. B*, 1984, **40**, 44–59.
53 J. P. Farges and A. Brau, *Phys. Status Solidi B*, 1974, **61**, 669–673.
54 S. Takagi, *J. Phys. Soc. Jpn.*, 1987, **56**, 1123–1126.
55 A. Berlie, I. Terry, Y. Liu and M. Szablewski, *J. Mater. Chem. C*, 2016, **4**, 6090–6095.
56 A. Berlie, I. Terry and M. Szablewski, *J. Mater. Chem. C*, 2018, **6**, 12468–12472.
57 A. Berlie, I. Terry, S. Cottrell, F. L. Pratt and M. Szablewski, *J. Phys.: Condens. Matter*, 2016, **29**, 025809.
58 L. Soriano, O. Pilone, M. D. Kuz'min, H. Vezin, O. Jeannin, M. Fourmigué, M. Orio and S. Bertaina, *Phys. Rev. B*, 2022, **105**, 064434.
59 M. Hase, I. Terasaki and K. Uchinokura, *Phys. Rev. Lett.*, 1993, **70**, 3651–3654.
60 M. Shaz, S. van Smaalen, L. Palatinus, M. Hoinkis, M. Klemm, S. Horn and R. Claessen, *Phys. Rev. B: Condens. Matter Mater. Phys.*, 2005, **71**, 100405(R).
61 A. Rohwer, M. Dressel and T. Nakamura, *Crystals*, 2020, **10**, 1085.
62 R. P. Groff, A. Suna and R. E. Merrifield, *Phys. Rev. Lett.*, 1974, **33**, 418–421.
63 G. A. Thomas, D. E. Schafer, F. Wudl, P. M. Horn, D. Rimai, J. W. Cook, D. A. Glocker, M. J. Skove, C. W. Chu, R. P. Groff, J. L. Gillson, R. C. Wheland, L. R. Melby, M. B. Salamon, R. A. Craven, G. De Pasquali, A. N. Bloch, D. O. Cowan, V. V. Walatka, R. E. Pyle, R. Gemmer, T. O. Poehler, G. R. Johnson, M. G. Miles, J. D. Wilson, J. P. Ferraris, T. F. Finnegan, R. J. Warmack, V. F. Raaen and D. Jerome, *Phys. Rev. B*, 1976, **13**, 5105–5110.
64 L. R. Melby, R. J. Harder, W. R. Hertler, W. Mahler, R. E. Benson and W. E. Mochel, *J. Am. Chem. Soc.*, 1962, **84**, 3374–3387.
65 L. R. Melby, *Can. J. Chem.*, 1965, **43**, 1448–1453.
66 J. P. Farges, A. Brau and F. Gutmann, *J. Phys. Chem. Solids*, 1972, **33**, 1723–1726.
67 M. Perić, M. Zlatar, S. Grubišić and M. Gruden-Pavlović, *Polyhedron*, 2012, **42**, 89–94.
68 M. K. Singh and G. Rajaraman, *Chem. – Eur. J.*, 2015, **21**, 980–983.
69 M. Arczyński and D. Pinkowicz, *Inorg. Chem.*, 2020, **59**, 13489–13501.
70 T. Barnes, J. Riera and D. A. Tennant, *Phys. Rev. B: Condens. Matter Mater. Phys.*, 1999, **59**, 11384–11397.
71 M. J. Konstantinovic, K. Ladavac, A. Belic, Z. V. Popovic, A. N. Vasil'ev, M. Isobe and Y. Ueda, *J. Phys.: Cond. Matter*, 1999, **11**, 2103.
72 D. C. Johnston, R. K. Kremer, M. Troyer, X. Wang, A. Klümper, S. L. Bud'ko, A. F. Panchula and P. C. Canfield, *Phys. Rev. B: Condens. Matter Mater. Phys.*, 2000, **61**, 9558–9606.
73 W. Duffy and K. P. Barr, *Phys. Rev.*, 1968, **165**, 647–654.
74 J. W. Hall, W. E. Marsh, R. R. Weller and W. E. Hatfield, *Inorg. Chem.*, 1981, **20**, 1033–1037.
75 O. Kahn, R. Hoffmann and M. Verdaguer, *Molecular magnetism*, Dover Publications, Garden City, New York, Dover edn, 2021.
76 J. C. Bonner and M. E. Fisher, *Phys. Rev.*, 1964, **135**, A640–A658.
77 (*a*) CCDC 2526797: Experimental Crystal Structure Determination, 2026, DOI: 10.5517/ccdc.csd.cc2qtblh; (*b*) CCDC 2526796: Experimental Crystal Structure Determination, 2026, DOI: 10.5517/ccdc.csd.cc2qtbkg.

